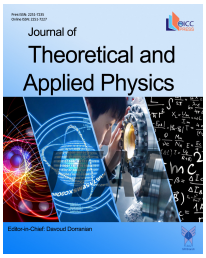

Volume 18, Issue 5, 182467 (1-13)

Journal of Theoretical and Applied Physics (JTAP)

https://dx.doi.org/10.57647/j.jtap.2024.1805.67

Impact of aluminum incorporation on thin-structured iron oxide nanoparticles: A comprehensive study

Dawood Salman Abd Al-Kader[1,*], Harakat Mohsin Roomy[2]

[1]*Ministry of Education, Directorate in Anbar, Anbar, Iraq.*
[2]*Ministry of Education, Baghdad, Iraq.*

[*]**Corresponding author:** dawodalany@gmail.com

Original Research

Received:
16 June 2024
Revised:
3 September 2024
Accepted:
27 September 2024
Published online:
30 October 2024

Abstract:

Our research attempts to investigate how doping affects the characteristics of thin iron oxide (Fe_2O_3) layers doped with various concentrations of aluminum (Al). The structure, morphology, and optical characteristics of the films were examined and evaluated in function to the Al doping level; "1%, 3%, 5%, and 7%, respectively". As indicated by several characterizations, Fe_2O_3 formation was confirmed as rhombohedral crystal system by X-ray diffraction, showing strong preferential orientation in one plane (104). Every peak observed in the un doped samples shows a continuous, slight shift towards lower values of $< 2\theta >$ with increasing aluminum "Al" doping levels. According to "AFM" data, as the doping ratio increases, the "grain size", "roughness rate", and "root mean square" all increase. The UV spectrum was analyzed to detect the optical properties. Al-doped Fe_2O_3 thin films exhibited lower optical absorption than pure film. On the other hand, the bandgap decreased in the range of $(2.31 - 2.2)$ eV with increasing Al content. As well as an increase in aluminum concentration is accompanied by increases in the "coefficient of absorption and extinction, refraction index".

Keywords: Thin layer; Iron oxide; Al doping; Structural and optical properties

1. Introduction

Transition metal oxides have unique properties that enable them to have applications, such as; biomedical, photonic devices, magnetic storage, and spintronic. On the other hand, the synthesis of transition metal oxides is difficult since they have different stoichiometric conformations [1]. Because of its excellent chemical and thermal stability, iron oxide is one of the more promising transition oxides of metals [2]. Iron oxide thin layer (Fe_2O_3) is considered to be one of the most efficient semiconductor materials. With significant technical potential for use in a variety of fields, Fe_2O_3 is a nontoxic, ecologically benign molecule with great electrochemical stability in addition to its good selectivity and sensitivity [3]. Iron oxide Fe_2O_3 has been shown to have significant third-order nonlinear optical susceptibility and a rapid reaction time, indicating its possible use in optical computing [4]. Fe_2O_3 is an excellent oxide material that absorbs visible light and can absorb up to 46% of solar spectrum energy with an optical bandgap of 2.2 eV [5]. Although iron oxide is a versatile choice for various applications due to its beneficial properties, however, pure iron oxide thin films have drawbacks such as poor optical properties and limited electrical conductivity [6]. Due to this, researchers are now investigating changes to improve these materials' functionality. Integration of aluminum (Al) into the Fe_3O_4 matrix is a potentially effective strategy to address the drawbacks of iron oxide thin films [7]. It is anticipated that doping iron oxide films with aluminum may change their electrical, optical, and structural characteristics, possibly improving their performance in a variety of applications. In other hand, the introduction of Al into the Fe_2O_3 lattice can induce strain, create defects, and alter the electronic structure, leading to changes in conductivity, band gap energy, and optical absorption characteristics [8, 9]. The effects of Al adding on Fe_2O_3 films' optical characteristics, particularly the absorption spectrum and band gap energy, have been reported with considerable variability. This inconsistency calls for comprehensive optical studies using standardized methodologies to accurately determine

the effects of doping. The impact of surface morphology, affected by Al doping, on the overall performance of Fe_2O_3 thin films has not been thoroughly investigated. Correlating Atomic Force Microscopy (AFM) studies with optical and electronic properties could offer important insights into the functional effects of surface roughness and texture [10, 11]. The properties of optical of the material must be understood for photosensitive applications; the absorption coefficient (k), band-gap "Eg", refractive index (n), and absorption coefficient (α), are some of these properties. The preparation parameters and models used to extract optical constants from the obtained data have an impact on the properties of optical of the thin layer. It is desirable to specify these properties with respect to the wavelength of light (or photon energy) [12]. Fe_2O_3 can be prepared using diverse techniques [13–18]. The Spray Pyrolysis approach has numerous advantages over other techniques, including; the fact that it doesn't require particular preparations before use, little cost, wide coverage, and tiny turnaround time [19]. The conditions for preparing Fe_2O_3 thin layers by the spray pyrolysis procedure often have a significant effect on the properties of these thin layers. Hence, a systematic investigation of the Physical features; (structural, optical, etc.) of Fe_2O_3 thin layers is required [20]. Thin layers are essential to current technology for a wide range of applications. Thin film technology is the cornerstone of the amazing advances in solid state devices. The great interest in the science and technology of thin film research has been fueled by the practicality of metal film optical characteristics as well as scientific curiosity about the behavior of two-dimensional solids [14]. Both scientific curiosity about the behavior of 2D solids and the practical application of metallic film optical characteristics have generated a significant deal of interest in the science and technology of thin film research [4]. Our research, a comprehensive investigation into synthesis, optical characterization, and structural analysis of Fe_2O_3 thin layers. Theses layers were doped with aluminum at concentrations varying from $1\% - 7\%$ and were meticulously prepared utilizing the spray pyrolysis. The study delved into the intricate alterations in the morphology, structure, and optical characteristics of iron nanoparticles to gain a nuanced understanding of material's behavior.

2. Experimental al details

2.1 Methods and materials

Spray pyrolysis works on the basis of the pyrolytic breakdown of the salts of the material that is to be deposited. Its primary components are an airtight fiber chamber, a hot plate, a liquid level monitor, a rotor for the spray nozzle, and a gas regulator value. Air was used as gas carrier, and the Spraying flow rate has been adjusted to approximately 3 milliliters per minute. The schematic diagram for the homemade spray pyrolysis system is displayed in Figure 1. A glass substrate is sprayed with an aqueous solution of 0.1 M $Fe(NO_3)_3{\cdot}9H_2O$ to deposit the Fe_2O_3 thin layer. The glass substrates with transmittance of 90% were utilized and cut into 5 cm $\times$ 1 cm pieces. Prior to deposition, the glass substrates were cleaned in an ultrasonic bath with deionized acetone for 10 minutes, followed by ethanol for 10 minutes, and finally with deionized water for 10 minutes. Substrates were then dried by blowing air and wiped with optical soft tissue before using for film deposition. In order to attain the best possible uniformity of the film and efficient heat transfer, a spotless glass slide is placed on a smooth, even surface that acts as a thermal conductor. To ensure proper adhesion and film quality, heat the substrates to the appropriate deposition temperature, typically 400 °C. The distance from the nozzle to the glass substrate was around 20 cm. Using the weighing method, the thickness of the layer was determined to be around 250 nm.

2.2 Preparation of precursor solution

2.02 gm of iron dichloride $FeCl_3.6H_2O$ (100% purity) were dissolved in 50 mL of methyl alcohol to prepare a pure solution. The resulting solution was yellow-orange in color. The solution concentrations used varied from 0.1 to 0.15 M. For doped iron oxide solution at different concentration; Add 0.056, 0.168, 0.280, and 0.392 g of Aluminum chloride ($Al_2Cl(OH)_5$) to the iron chloride solution to achieve 1%, 3%, 5%, 7% molar respectively doping. With the spray nozzle, atomize the precursor solution. The air carrier gas aids in transporting the tiny droplets to the heated substrate. Iron oxide thin films are formed when the precursor droplets undergo pyrolytic decomposition upon contact with the heated substrate. The solvent evaporates, leaving behind a solid film. Improve the crystallinity and film qualities by annealing the deposited films for 1.5 hour at 400 °C in oxygen.

2.3 Characterization techniques

Characterization of the prepared thin layers was performed using XRD diffraction, UV-Vis spectroscopy, and atomic force microscopy. The crystalline structures and phase formation of the thin films were carried out using X-Ray diffraction "XRD, with Shimadzu X-ray diffraction analyzer with a Cu Kα source (1.54 A) at 40 Kv and 30 mA". The X-rd. patterns were investigated for prepared samples that located onto glass substrate and analyzed from "30° – 80°" of 2. To study the optical properties of prepared thin films, the optical performance spectra in the wave-length range of $(400 - 900)$ nm were investigated with

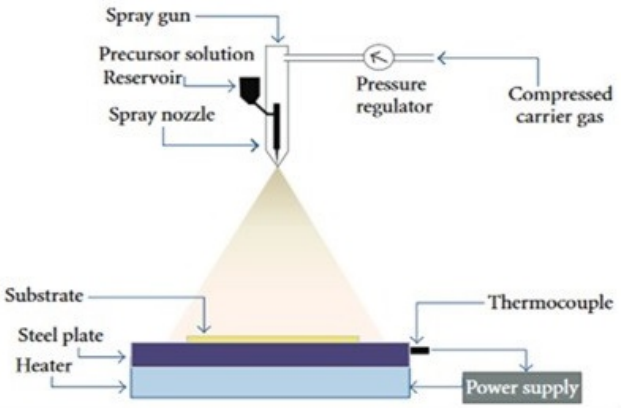

Figure 1. The scheme of the CSP setup.

"a UV/VIS-Spectroscopy double beam spectrophotometer (Visible1900) built by (Sgimadzu, Japanese Co.)". Atomic Force Microscopy (AFM) is a microscopy technique used to describe topography, morphology, the surface texture, roughness, and particle -size distribution of nanoparticles. The instrument is utilized for type (AA3000 Scanning Probe Microscope SPM, tip NSC35/AIBS) inspection.

3. Results and discussion

3.1 Properties of structural

XR- diffraction patterns of Fe_2O_3 thin layers doped-Al, and undoped with varying Al ratios are shown in Figure 2. The XRD patterns exhibit peaks centered at 2θ: values of 24.185°, 33.176°, 35.72°, 49.51° and 54.036° conforming to the (012), (104), (110), (024) and (116) lattice planes respectively. The polycrystalline nature of all the samples and their rhombohedral Fe_2O_3 phase structure, with (104) being the preferred orientation are consistent with other research findings [21]. There were no secondary phases found that matched other metal oxides. Also the finding indicates that the increasing the Al concentration to 3% led to an initial rise in the intensity of the (104) peak. It is also significant to observe that, even while orientation (104) is still preferred, there was a propensity for crystallites to grow along the (110) plane once Al atoms were added. All detected peaks in the undoped samples shift slightly to lower 2θ values with increasing concentrations of Al doping as illustrated in Figure 2 for the doped samples. Furthermore, the XRD data demonstrated that as the Al content varies, the average crystallite size changes. The diffraction data matches the JCPDS (JCPDS NO. 89-8104) standard for Fe_2O_3, helping us identify the different peaks in our samples. Table 1 displays the structural parameters calculated from the diffraction peaks (104), (110), (024), and (116), which align with the JCPDS standard. The average crystallite size "D" of the synthetic samples was considered by the equation D-scherrer [22]:

$$D = \frac{K\lambda}{\beta \cos\theta} \tag{1}$$

where D denotes the crystallite size, λ is the wave length of X-ray which used, "K" is the shape factor, "β" is the Half Maximum of Full Width of the peak diffraction and "θ" is the Bragg diffraction angle. Table 1 illustrates how the size of crystallite rose from 18.26 to 30.8 nm as the aluminum percentage increased. The important variation in size of crystallite is due to an increase in the amount of reaction between the Fe_2O_3 and Al. The average atom mobility and diffusion length rise with increasing Al content, and Al is therefore predicted to be readily trapped by Fe_2O_3. As a result, the fusion phase will not be kinetically restricted, and the final size of the crystal grains will grow. When the particles reach the substrate, they experience more collisions [21].

The following relationships established the parameters of the Fe_2O_3 thin layers, including the dislocation density (δ), micro-strain ($\acute{\varepsilon}$), and stacking fault (SF) [22];

$$\delta = \frac{1}{D^2} \tag{2}$$

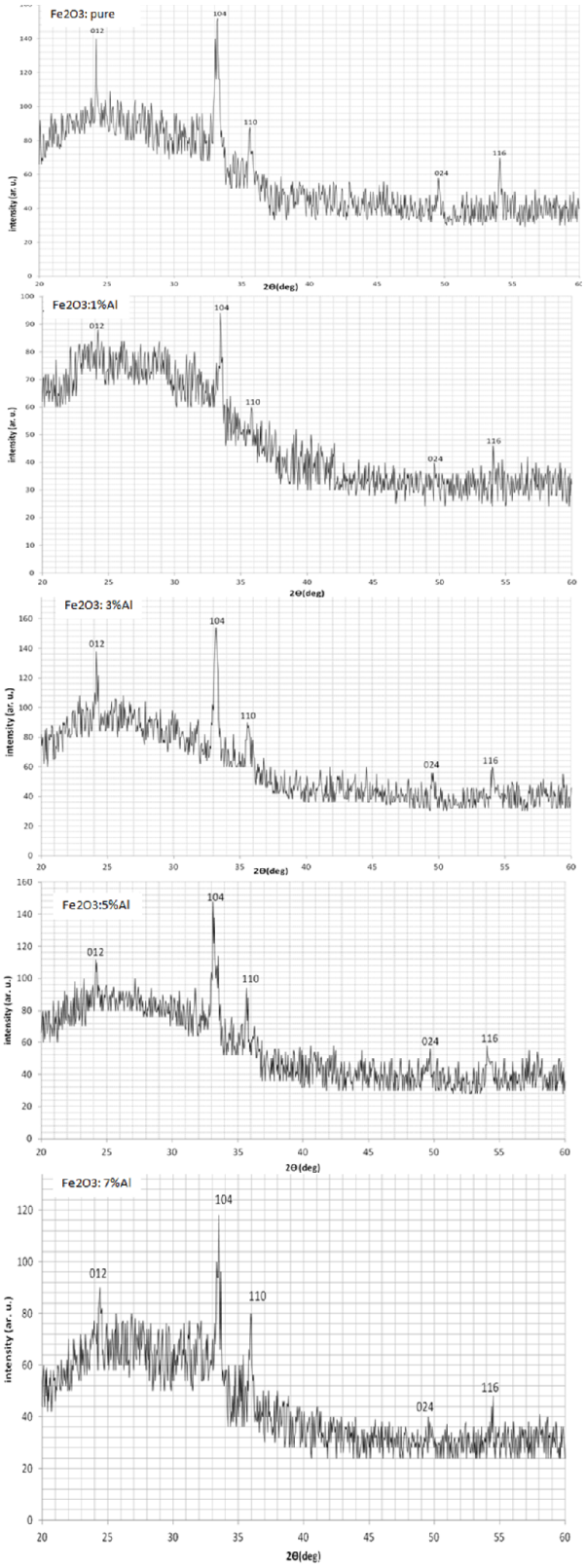

Figure 2. XR diffraction patterns of Fe_2O_3 thin layers with varying compositions that are un-doped and Al-doped.

$$\acute{\varepsilon} = \frac{\beta}{4\tan\theta} \tag{3}$$

$$SF = \frac{2\pi^2\beta}{45(3\tan\theta)^{0.5}} \tag{4}$$

Table 2. Evaluation the dislocation density (δ) and micro-strain ($\acute{\varepsilon}$), which are measures of defects in the films, based on Equations (2), (3) and (4) respectively by employing compounds of (Fe_2O_3: Al) at (1, 3, 5, and 7%) concentrations. The number of defects in a crystal is indicated by the dislocation density. As seen in Table 2, the values of micro-strain and the dislocation density increase with increasing aluminum content in the films, where the micro-strain depends directly on the lattice constant. Growing aluminum concentration in the thin layers led to a rise in the number of crystallites per unit surface area.

The Williamson-Hall method (WH) is a simple way to distinguish between the contributions of lattice strain and crystallite size to peak broadening in (XRD) patterns. This analysis makes the assumption that the line broadening is caused by the crystallite size (D) and lattice strain (ε). The

Table 1. Structural parameters of Fe_2O_3-doped Al films with different doping (1, 3, 5 and 7%).

Sample	$(2\theta)^\circ$	d_{hkl} (Å)	(hkl)	I (ar.u)	T_c(hkl)	a_0 (Å)	C_0 (Å)	D (nm) W-Hall	D (nm) Scherer
Fe_2O_3 (ASTM)	24.125	3.686	012	25		5.035	13.748		
	33.114	2.703	104	100					
	35.611	2.519	110	50					
	49.416	1.842	024	40					
	54.003	1.696	116	60					
Fe_2O_3 pure	24.185	3.677	012	44	0.7	5.023	13.701	19.8	18.26
	33.176	2.69	104	100	1.23				
	35.72	2.511	110	88	1.23				
	49.516	1.839	024	58	1.015				
	54.036	1.695	116	70	0.817				
Fe_2O_3: 1% Al	24.198	3.675	012	70	0.73	5.024	13.731	21.66	20.4
	33.213	2.695	104	100	2.07				
	35.71	2.512	110	60	0.88				
	49.653	1.834	0240	40	0.74				
	54.05	1.69	116	46	0.573				
Fe_2O_3: 3% Al	24.212	3.672	012	40	0.86	5.025	13.713	21	21.6
	33.241	2.693	104	100	1.38				
	35.705	2.512	110	40	0.69				
	49.61	1.836	024	56	1.2				
	54.09	1.694	116	60	0.86				
Fe_2O_3: 5% Al	24.17	3.679	012	43	0.835	5.028	13.708	23.1	22.74
	33.231	2.693	104	100	1.436				
	35.68	2.514	110	45	0.751				
	49.62	1.83	024	56	1.17				
	54.05	1.695	116	58	0.81				
Fe_2O_3: 7% Al	24.351	3.652	012	90	0.625	5.02	13.691	35.5	30.82
	33.341	2.685	104	100	2.25				
	35.743	2.510	110	80	1				
	49.54	1.838	024	40	0.625				
	54.08	1.694	116	48	0.5				

following equation can be used to express the WH technique [23].

$$\beta_{hkl}\cos\theta = \frac{k\lambda}{D} + 4\varepsilon\sin\theta \quad (5)$$

The practical application of the WH plotting involves the construction of plotting $< \beta_{hkl}\cos\theta >$ against $< 4\sin\theta >$. When the sample shows a homogenous distribution for the lattice strain and crystallite size, the "WH" plot displays a straight line. The fitting of the values was linear. The point where the line intercepts the y-axis equals size of crystallite and the lattice strain from the slope of x-axis. Figure 3 shows the graph plotted by WH analysis. From Equation (5), it is evident that the diffraction peak's broadening affects the size of the crystallite (D). As the size of the crystallite decreases, the broadening increases, which also affects the lattice strain (βstrain). Fig. 3 illustrates how the crystallite size and micro-strain depend on the amount of Al. The crystallite size for the undoped Fe_2O_3 sample, as shown in Table 1, is estimated to be approximately 19.8 nm based on W-Hall plots, and it grew dramatically to approximately 35.5 nm at 7% AL, moreover, the resulting sample exhibits the lowest micro-strain and dislocation density as shown in Table 2. This improvement of crystallite size is probably result of less of lattice imperfections in the film, such as micro-strain and fraction of grain boundaries [24]. The average crystal size was calculated on the diffraction peaks

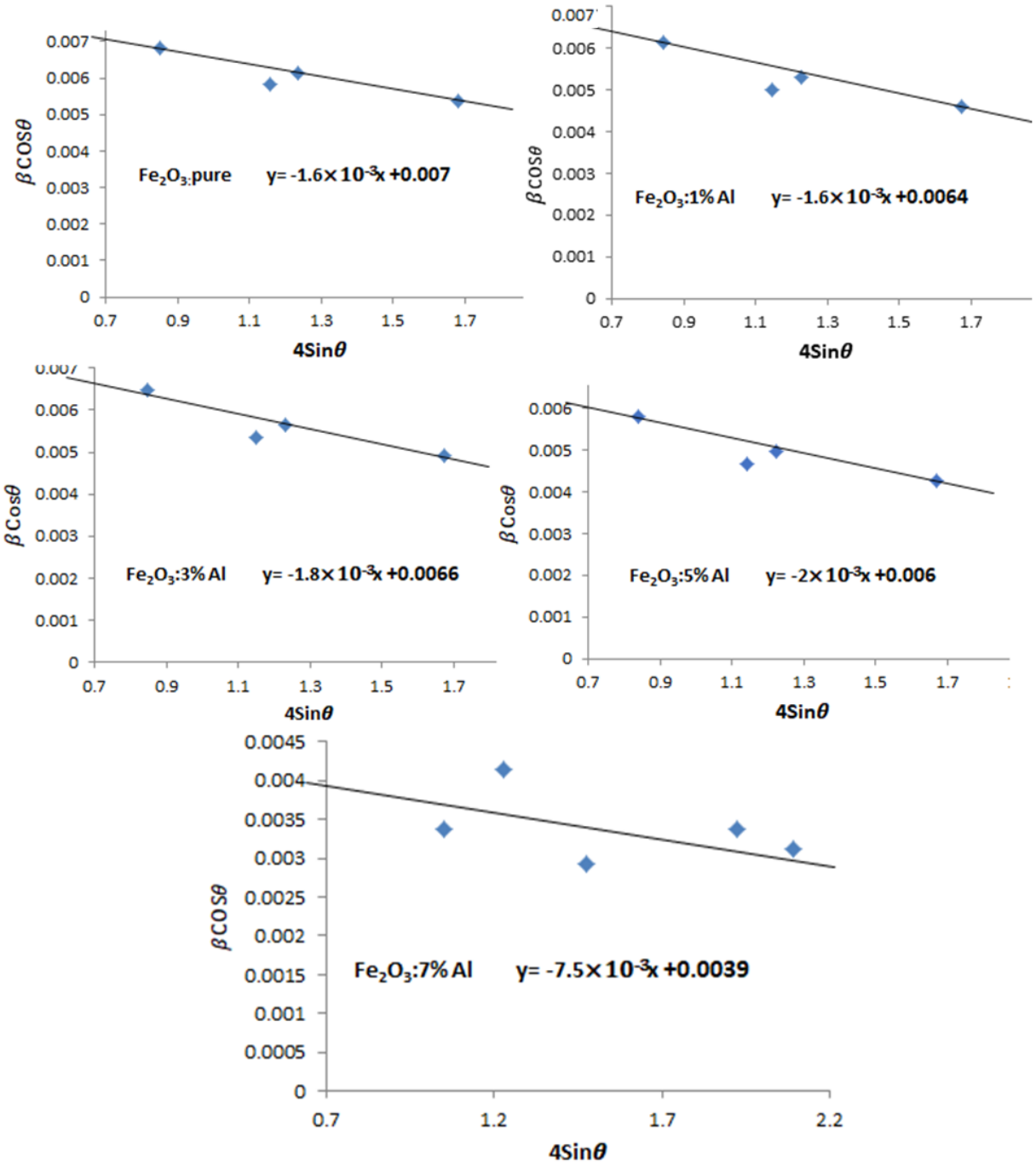

Figure 3. Williamson Hall plots of Al-doped Fe_2O_3 nanostructured with diverse Al substances.

(104), (110), (024), and (116) using the Scherer equation. The average crystal size was then compared to the W-Hall diagram results, which demonstrated a clear convergence in the crystal size values and an increase in the size of the crystals.

The preferred direction of crystallization, which usually develops in a material due to an increased tendency for crystallization to proceed in a certain direction, is the most suitable direction in the texture of that material Tc. When the texture coefficient is one, then the crystallization occurs randomly within the sample. However if Tc(hkl), the sample will crystallize in a certain (hkl) direction [25]. The number of oriented crystals increases periodically as the texture coefficient value rises. The following formula [26] is used to estimate the texture coefficient value "Tc";

$$Tc(\text{hkl}) = \frac{[I(\text{hkl})/I_0(\text{hkl})]}{[Nr^{-1}\Sigma I(\text{hkl})/I_0(\text{hkl})]} \tag{6}$$

where, P(hkl) is the coefficient of texture from the plane specified by Miller-Indices (hkl), I : is the intensity of the (hkl) plane from X-ray diffraction (XRD), I_0 is the standard intensity for the (hkl) plane from a reference material with random orientation, N_r: the reflection number. Table 2 lists the estimated values of Tc for the four significant diffraction peaks (110), (116), (024), and (104). When the texture coefficient increases or decreases from unity "it signifies a greater or lesser degree of preferred orientation along a particular film plane in comparison to pure Fe_2O_3". Thus, as comparison to ideal values, a higher (lower) texture coefficient value really correlates to an increase (reduction) in planar density along a specific crystal plane. Hence, the texture analysis shows that pure Fe_2O_3 has a high degree of texture, with the highest intensity (I) along the (104) plane. with the substitution of Al in Fe_2O_3, the texture coefficient of (104) plane increases remarkably with concomitant decrease in (110) planar density in case of 1% wt W-doped thin films. The same changes are observed for 3, 5 and 7% wt. Al doped samples i.e. coefficients of texture of (104) is slightly higher than (110) plane and both are near unity.

3.2 Morphological properties

The thin film surface morphology of the prepared samples was revealed via AFM analysis, understanding how atoms are distributed and arranged on surfaces, as well as the differences, isotropy, or features related to each individual atom, is important for studying film surfaces. Figure 4 displays 3D representations of pure Fe_2O_3 and Al:Fe_2O_3 thin layers over an area (900 nm × 900 nm) using AFM images. The growth distribution of granular particles on the surface of the deposited films is shown in the figure. Each layer shows the presence of grains, confirming the poly-crystalline nature of the developed thin layers. The images confirm that the Fe_2O_3 films have a smooth surface morphology that decreases with increasing aluminum doping, i.e, the growing of small grains with rising Al% leads to an increase in roughness and root mean square layers, with more doping it showed a homogeneous and consistent texture. An increase in aluminum doping leads to the growth of crystallites and film thickness, resulting in an increase in surface roughness from 3.12 nm to 16.75 nm, as shown in Table 3. Consequently, the band gap narrowing is

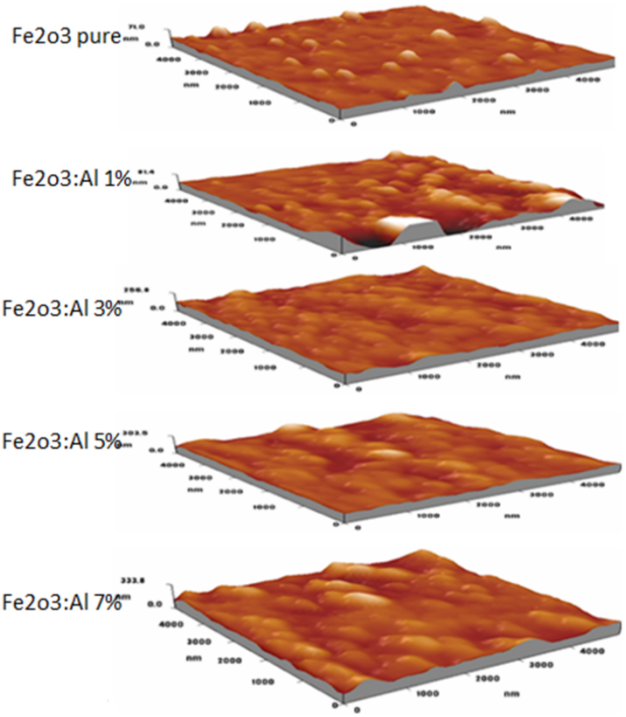

Figure 4. AFM information.

Table 2. Micro-strain ($\acute{\varepsilon}$) and the dislocation density (δ) for pure Fe_2O_3 and Fe_2O_3: Al thin films for preferred orientation (104).

Sample	$(2\theta)^\circ$	d_{hkl} (Å)	Micro $\times 10^{-3}$ Strain (Scherer)	Strain $\times 10^{-3}$ W-Hall	δ (nm)$^{-2}$ $\times 10^{-3}$	Stacking fault $\times 10^{-3}$	hkl
Fe_2O_3 pure	33.176	2.698	2.731	1.6	6.747	5.284	104
Fe_2O_3: 1% Al	33.213	2.695	2.348	1.6	4.987	4.54	104
Fe_2O_3: 3% Al	33.241	2.693	1.773	1.8	2.844	3.427	104
Fe_2O_3: 5% Al	33.231	2.694	1.701	2	2.618	3.288	104
Fe_2O_3: 7% Al	33.341	2.6857	1.078	0.75	1.052	2.08	104

caused by the existence of aluminum ions, which coincide with oxygen forming its own oxide AlO. These are crystal defects that are associated with rising Urbache energy. The reduction in size of crystallite was detected due to the existence aluminum oxide in the tin films. Doping allows for the adjustment of optical parameters; the absorptivity of Al-doped Fe_2O_3 films is also enhanced due to increased aluminum doping. However, the increase in surface roughness causes the extinction coefficient of the film to become larger. The "grain size, surface roughness, and root mean square (RMS)" of all thin layers are listed in Table 3. These results are aligning with the XRD data [27].

Using a "UV-Vis-NIR" spectrophotometer, the impact of Al-doping on the characteristics of optical of the Fe_2O_3 thin layers was measured at wavelengths between 300 and 900 nm. The absorbance, reflectance and transmittance spectra of un-doped and Al-doped Fe_2O_3 thin films (1, 3, 5 and 7 at%) are presented in Figure 5. Figure 5 (A) shows that all of the thin layers exhibit substantial absorption at wavelengths a lesser of 450 nm, due to interactions that occur between the incident photon and the material at short wavelengths, leading to increased absorption. Then, the absorbance declines as the wave-length rises. This is explained by the fact that incident photons of high wavelengths will transmit instead of interact with atoms due to insufficient energy [28]. Additionally, the increase in absorption is clearly correlated with the increase in the aluminum ratio, this confirms the entry of aluminum atoms into the crystal structure of the produced thin layer. Figure 5 (A) illustrates that aluminum doped Fe_2O_3 exhibits slight absorption in the visible spectrum and no absorption in the infrared. Absolutely, as the Al doping concentration increases, there's a potential for the absorption edge to shift to longer wave lengths (red shift). This shift is the result of dopant atoms causing modifications to the material's electrical structure. Increased doping concentrations have the potential to change the band structure, which would cause the absorption edge to shift to lower energy levels and extend into the infrared spectrum. This phenomenon is frequently seen in doped materials, and it has a big impact on their electrical and optical characteristics. Equation (7) is used to compute the optical transmittance of Fe_2O_3 thin layers deposited with varying amounts of aluminum [29];

$$T = e^{-2.303A} \tag{7}$$

Figure 5 (B) displays the spectra transmittance of the aluminum-doped and pure Fe_2O_3 thin layers. The spectra have the same overall shape and are divided into two regions. In the strong transmittance region, which corresponds to significant absorption ($\lambda < 500$ nm), the transmittance begins to cancel out at wavelength lower than 500 nm. In contrast, the transmittance declines as the proportion of aluminum rises. This phenomenon might result from a decrease in surface roughness. Which decreases the quantity of light scattered on the surface Figure 5 (C) shows the reflectance spectra for the pure and aluminum-doped Fe_2O_3 thin films. The plane showed a sharp diminution in reflectance at wave-lengths less than 450 nm, while it regularly decreased at wavelengths greater than 450 nm. In addition, the reflectance increased with decreasing aluminum doping. The coefficient of absorption "α" for doped and pure Fe_2O_3 thin layers' deposition with diverse concentrations of aluminum was computed using the following formula [30].

$$\alpha = \frac{2.303 \times A}{t} \tag{8}$$

where: A is the optical absorption and t is the thickness of the thin layers.

The absorption coefficient in Figure 5 (D) shows great values $\alpha > 10^4$ cm^{-1} showing a strong possibility of a direct transition [27], and then α rises with increasing wave-length. The (α) increases as the aluminum concentration rises. This is because when the doping ratio increases, the energy gap contracts. We observe that the films have poor ultraviolet transparency and high transparency in the visible area. With an absorption edge ranging from 380 nm to 420 nm, contingent upon the deposition settings, the transmittance exceeds 60%. The fringes of interference of the transmittance spectra confirmed the smooth, highly reflective surface of the thin layers, devoid of any match scattering or absorption loss. The Burstein-Moss effect is primarily responsible for the blue shift, a slight change in the absorption edges of doped Fe_2O_3 toward shorter wavelengths [31]. Equation (9) can be used to obtain the "n" for doped and pure Fe_2O_3 layers deposition with varying concentrations of aluminum [32].

$$n = \sqrt{\frac{4R - K^2}{(R-1)^2}} - \frac{(R-1)}{(R+1)} \tag{9}$$

Table 3. Surface topography of the intended films.

Sample	Average diameter (nm)	Surface roughness (nm)	RMS (nm)
Fe_2O_3 pure	76.71	3.12	4.71
Fe_2O_3: 1% Al	88.32	6.85	10.51
Fe_2O_3: 3% Al	112.37	10.88	13.89
Fe_2O_3: 5% Al	123.63	16.57	21.82
Fe_2O_3: 7% Al	131.42	20.48	26.61

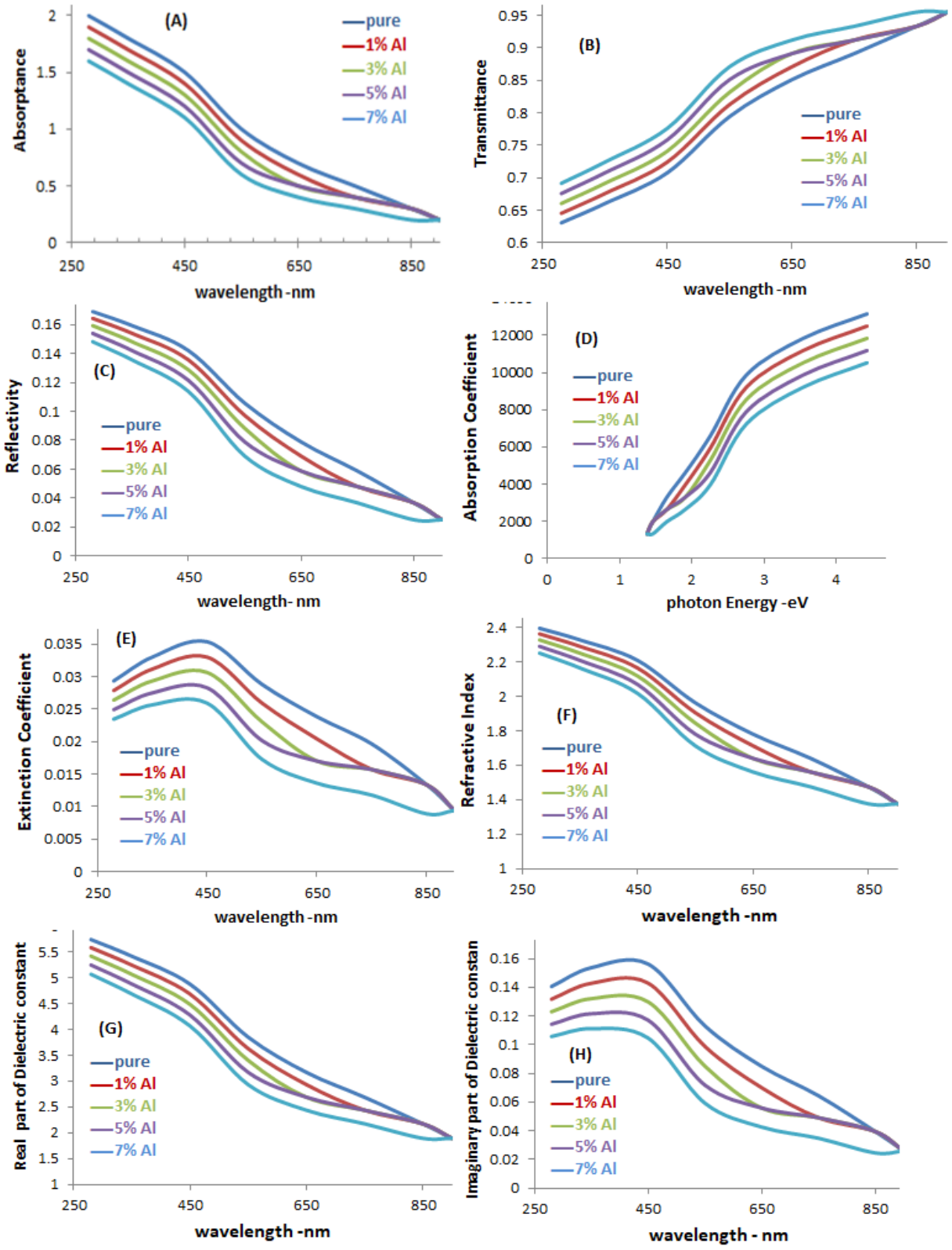

Figure 5. (A) Absorbance, (B) Transmittance, (C) Reflectance, (D) Absorption coefficient vs wavelength. Extinction coefficient, (F) refractive index, (G) real dielectric constant, (H) imaginary dielectric constant vs. wavelength

where: R is the reflectance which can be determined by:

$$R = \frac{(n-1)^2}{(n+1)^2} \tag{10}$$

where: (k) is the coefficient of extinction. Figure 5 (F) illustrates how the refractive index varies with wave-length for both doped and pure Fe_2O_3 thin layers at various aluminum concentration in the $270-900$ nm range. The figure below shows that as the aluminum concentration increases, the

refractive index (n) decreases. This behavior can be understood in terms of how increases the aluminum concentration causes the prepared samples to become minus dense (reducing the density of packing) and to undergo a variation in structure of crystalline. This in turn rises the velocity of light propagation through the sample, which decreases the (n) values. The (k) is the imaginary portion of the complex refraction index N. Equation (9) may be used to compute the (k) for both doped and pure Fe_2O_3 thin layers deposited with varying concentrations of aluminum [29].

$$k = \frac{\alpha\lambda}{4\pi} \tag{11}$$

Figure 5 (E) illustrates the correlation between the wavelength and extinction coefficient of the doped and pure Fe_2O_3 thin layers that were deposited. For all the prepared samples, it is generally evident that the (k) declines as the wave-length (λ) increases, while, the (k) increases as the aluminum doping ratio increases. The coefficient of extinction exhibits behavior comparable to that of the coefficient of absorption. This is explained by the same cause as before. As the aluminum content increases, the absorbance decreases, thereby reducing the optical energy gap. Figures 5 (G), 5 (H) displays the dielectric constant s real and imaginary parts (ε_r and ε_i) versus wave-length in the range of $(270-900)$ nm for the doped and pure Fe_2O_3 thin layers. The behaviors of (ε_r) is comparable to that of the (n) since (k) has a lower value than (n), while the (k) values mostly determine (ε_i). When the ratio of aluminum increases, (ε_r) and (ε_i) decrease. It can be observed that the real part has a higher value than the imagined part. As seen from the above, an increase in the doping concentration causes the localized state to reorganize, which decreases the conductivity of the film while increasing the fixed real isolation [33].

Due to the exceptional importance of the optical band-gap and the energy values of the materials under study, there have been numerous attempts to analyze and calculate the energy required for the electronic transition from the valence-band level to the conduction-band level. Based on the following experimental relationship, these models and assumptions are based on the value of the absorption coefficient α, which appears as an exponential function of the photon energy near the band edge in the semiconductor [34]:

$$\alpha h\nu = \beta(h\nu - E_{opt})^y \tag{12}$$

where β is a constant named the band tailing parameter, E_{opt} is the energy of the optical bandgap, then, y is the power factor of the transition mode which depends on the type of the material. If it is direct or indirect, allowed or forbidden. The energy of band-gap is determined from the graph of photon energy $h\nu$ vs.$(\alpha h\nu)^{1/y}$. As shown in Figure 6. The optical energy-gap values "E_{opt}" for the doped and pure and Fe_2O_3 thin layers were obtained by graphing $(\alpha h\nu)^2$ as a function of $(h\nu)$. By extending the curve s straight line and intersecting it with the x-axis, the energy gap of the resulting thin layers can be determined. Fig. 6 displays that the energy gap of pure Fe_2O_3 is 2.31 eV, which decides with the outcome shown in reference [35]. Introducing a small amount of aluminum into iron oxide will slightly modify the electronic structure. Aluminum atoms can replace some of the iron atoms in the lattice, introducing additional states in the band-gap. This often leads to a slight reduction in the band-gap due to the creation of impurity states. With more Aluminum atoms, the impurity states increase, further narrowing the band-gap. The band-gap reduction becomes more noticeable. As the concentration of aluminum increases, the density of states inside the optical gap increases, leading to an increase from the secondary levels and a contraction of the tail region. This narrowing of the optical energy-gap contributes to a decrease in the energy gap and ultimately increases the electronic transfer, the material's overall electronic properties are significantly altered. Table 4 displays the energy-gap values of the fabricated thin layers.

When impurities are added to a semiconductor, the band gap will frequently exhibit band tailing. Phonon interactions and the existence of a tail absorption profile that coincides with the empirical Urbach law [36]:

$$\ln\alpha = \ln\alpha_0 + \frac{h\nu}{E_U} \tag{13}$$

$$E_U = \alpha\left(\frac{d\alpha}{d(h\nu)}\right)^{-1} \tag{14}$$

where $\alpha(h\nu)$ represents the experimentally deduced optical absorption profile and α_0 is a constant the E_U refers for the states' band tail width in the prohibited band. The reciprocal values of the slopes of the linear portion of the plots of $\ln(\alpha)$ versus "$h\nu$" are used to calculate the E_U values. As shown in Fig. 7. The energy connected to the microstructural lattice disorder suggests that the addition of aluminum reduces the

Table 4. Values of energy gap and Urbach energy for pure and doped Fe_2O_3 thin films.

Sample	Energy gap (eV) of allowed direct transition	Urbach energy (meV)
Fe_2O_3 pure	2.31	553
Fe_2O_3: 1% Al	2.27	676
Fe_2O_3: 3% Al	2.22	713
Fe_2O_3: 5% Al	2.2	784
Fe_2O_3: 7% Al	2.23	827

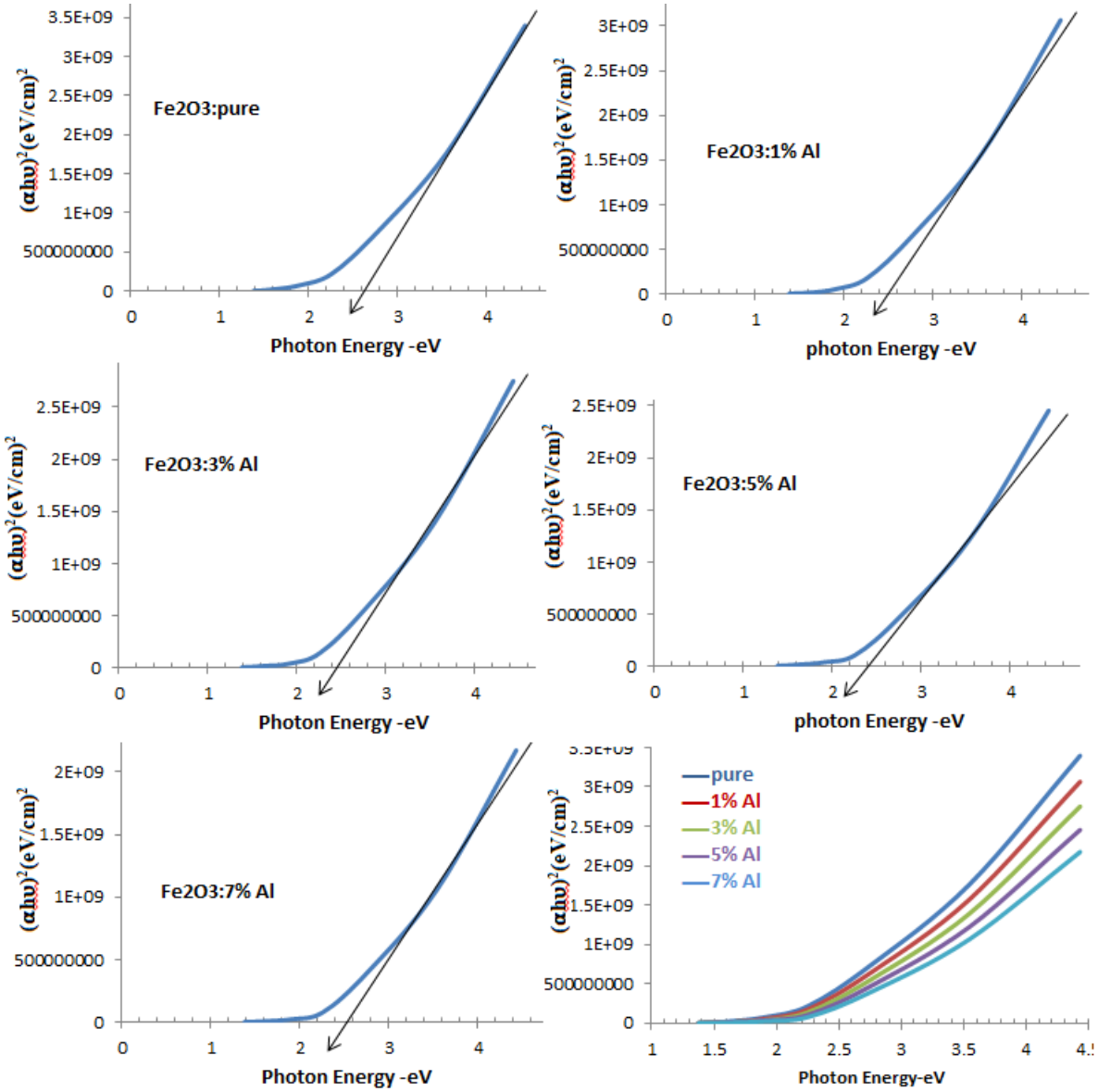

Figure 6. The estimated band gap (Eg) for pure and doped Fe_2O_3.

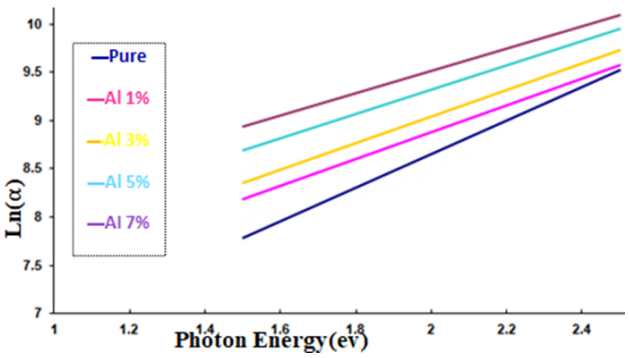

Figure 7. The variation in $\ln(\alpha)$ as a function of the energy gap for pure and doped Fe_2O_3.

α content of defects and disorder in the Fe_2O_3 thin film. The energy gaps of the allowed direct-transition (Eg) and Urbach energy (E_U) are presented in Table 4.

4. Conclusion

Thin layers of nanostructured pure Fe_2O_3 and Al: Fe_2O_3 thin layers were deposited by the CSP technique on a glass substrate. From results of (XRD), revealed that all the thin layers were crystallized in a rhombohedral structure with (104) as the favored plane orientation with an almost constant slight shift toward larger angles when the doping rate increased. The (AFM) images show that the average surface roughness and root mean square (RMS) of the thin layers increase with in increasing Al concentration, and the crystallite size increases with increasing doping concentration from $12.17 - 30.8$ nm. These outcomes agree with the XRD results. The optical characteristics demonstrate that the band gap decreasing Al concertation and the band-gap diverse from 2.61 to 2.41 eV for the direct-transition. This could lead to a decrease in the energy gap by raising the density of localized permitted states in the energy band gap close to the conduction band. The

addition of aluminum raises the carrier concentration, which shifts the Fermi level and prevents some of the higher states. Furthermore, the outcomes show that the optical transmittance T increases as the doping concentration rises, and the lowering of optical constants with increasing dopant ratio, such as the extinction coefficient K index of reflection n and dielectric constants.

Acknowledgments

The authors would like to thank the National Research Foundation of South Africa for funding under research grant number CSRP2204214088.

Authors contributions
The authors did all simulations and compiled the manuscript.

Availability of data and materials
All data presented in this article are available on request.

Conflict of interests
The authors declare that they have no known competing financial interests or personal relationships that could have appeared to influence the work reported in this paper.

References

[1] R. B. Ayed, M. Ajili, J. M. Garcia, A. Labidi, and N. K. Turki. "Physical properties investigation and gas sensing mechanism of Al: Fe_2O_3 thin films deposited by spray pyrolysis.". *Superlattices and Microstructures*, **129**, 2019. DOI: https://doi.org/10.1016/j.spmi.2019.03.002.

[2] Z. Lei, J. M. Lee, G. Singh, C. I. Sathish, X. Chu, A. H. Al-Muhtaseb, A. Vinu, and J. Yi. "A Recent advances of layered-transition metal oxides for energy-related applications.". *Energy Storage Materials*, **36**, 2021. DOI: https://doi.org/10.1016/j.ensm.2021.01.004.

[3] S. S. Shinde, R. A. Bansode, C. H. Bhosale, and K. Y. Rajpure. "Physical properties of hematite, -Fe_2O_3 thin films: application to photoelectrochemical solar cells.". *Journal of Semiconductors*, **32**, 2011. DOI: https://doi.org/10.1088/1674-4926/32/1/013001.

[4] J. Krysa, M. Zlamal, S. Kment, M. Brunclikova, and Z. Hubicka. "TiO_2 and Fe_2O_3 films for photo electrochemical water splitting. ". *Molecules*, **20**:1046–58, 2015. DOI: https://doi.org/10.3390/molecules20011046.

[5] K. A. Mishjil, N. H. Numan, M. S. Othman, N. F. Habubi, N. N. Jandow, and H. G. Rashid. "A comparative study of structural and optical properties of Al-doped Fe_2O_3 films: experimental and DFT approach. ". *MJPAS*, **1**, 2023.

[6] M. S. Chavali and M. P. Nikolova. "Metal oxide nanoparticles and their applications in nanotechnology. ". *SN Applied Sciences*, **1**:607, 2019. DOI: https://doi.org/10.1007/s42452-019-0592-3.

[7] R. C. Bradley. "Optimisation of Fe_3O_4 thin films and nanostructures for atom trapping applications. ". *University of Sheffield ,Doctor of Philosophy*, , 2017.

[8] L. Chen, C. Shi, X. Li, Z. Mi, D. Wang, H. Liu, and L. Qiao. "Strain effect on electronic structure and work function in α-Fe_2O_3 films.". *Materials*, **10**:273, 2017. DOI: https://doi.org/10.3390/ma10030273.

[9] A. Kumar, R. Kumar, N. Verma, A. V. Anupama, H. K. Choudhary, R. Philip, and B. Sahoo. "Effect of the band gap and the defect states present within band gap on the non-linear optical absorption behaviour of yttrium aluminium iron garnets. ". *Optical Materials*, **108**:110163, 2020. DOI: https://doi.org/10.1016/j.optmat.2020.110163.

[10] R. B. Ayed, M. Ajili, J. M. Garcia, A. Labidi, and N. K. Turki. "Physical properties investigation and gas sensing mechanism of Al: Fe_2O_3 thin films deposited by spray pyrolysis. ". *Superlattices and Microstructures*, **129**:91–104, 2019. DOI: https://doi.org/10.1016/j.spmi.2019.03.002.

[11] E. P. da Silva, M. Chaves, G. J. da Silva, L. B. de Arruda, P. N. Lisboa-Filho, S. F. Durrant, and J. R. R. Bortoleto. "Al-doping effect on the surface morphology of ZnO films grown by reactive RF magnetron sputtering. ". *Materials Sciences and Applications*, **4**:761–767, 2013. DOI: https://doi.org/10.4236/msa.2013.412096.

[12] J. Dvo˘rák, J. rí Vohánka, V. Buršíková, D. Franta, and I. Ohlídal. "Optical characterization of inhomogeneous thin films deposited onto Non-absorbing substrates.". *Coatings*, **13**:873, 2023. DOI: https://doi.org/10.3390/coatings13050873.

[13] T. A. Lastovina, A. P. Budnyk, M. A. Soldatov, Y. V. Rusalev, A. A. Guda, A. S. Bogdan, and A. V. Soldatov. "Microwave-assisted synthesis of magnetic iron oxide nanoparticles in oleylamine– oleic acid solutions. ". *Mendeleev Communications*, **27**:487–489, 2017. DOI: https://doi.org/10.1016/j.mencom.2017.09.019.

[14] A. Lassenberger, T. A. Grnewald, P. D. J. van Oostrum, H. Rennhofer, H. Amenitsch, R. Zirbs, H. C. Lichtenegger, and E. Reimhult. "Monodisperse iron oxide nanoparticles by thermal decomposition: Elucidating particle formation by second-resolved in situ small-angle X-ray scattering.". *Chem. Mater.*, **29**:4511–4522, 2017. DOI: https://doi.org/10.1021/acs.chemmater.7b01207.

[15] J. B. Mamani, L. F. Gamarra, and G. E. de S. Brito. "Synthesis and characterization of Fe_3O_4 nanoparticles with perspectives in biomedical applications.". *Mater. Res.*, **17**, 2014. DOI: https://doi.org/10.1590/S1516-14392014005000050.

[16] H. Hayashi and Y. Hakuta. "Hydrothermal synthesis of metal oxide nanoparticles in supercritical water. ". *Materials (Basel)*, **3**:3794–3817, 2010. DOI: https://doi.org/10.3390/ma3073794.

[17] P. L. Hariani, M. Faizal, R. Ridwan, M. Marsi, and D. Setiabudidaya. "Synthesis and properties of Fe_3O_4 nanoparticles by Co-precipitation method to removal procion dye . ". *Int. J. Environ. Sci. Dev.*, **4**:336–340, 2013.

[18] R. Alexandrescu, V. Bello, V. Bouzas, R. Costo, and F. Dumitrache. "Iron oxide materials produced by laser pyrolysis. ". *AIP Conf. Proc.*, **1275**:22–25, 2010. DOI: https://doi.org/10.1063/1.3505075.

[19] H. Ghaith Jihad. "Synthesis and characterization of α-Fe_2O_3 nanoparticles prepared by PLD at different laser energies .". *Iraqi Journal of Science*, **62**, 2021. DOI: https://doi.org/10.24996/ijs.2021.62.11.11.

[20] J. Dvo ˇ rák, J. rí Vohánka, V. Buršíková, D. Franta, and I. Ohlídal. "Optical characterization of inhomogeneous thin films deposited onto Non-absorbing substrates.". *Coatings*, **13**:873, 2023. DOI: https://doi.org/10.3390/coatings13050873.

[21] A. Rufus, N. Sreeju, and D. Philip. "Size tunable biosynthesis and luminescence quenching of nanostructured hematite (α-Fe_2O_3) for catalytic degradation of organic pollutants. ". *J. Phys Chem Solids*, **124**:221–234, 2019. DOI: https://doi.org/10.1016/j.jpcs.2018.09.026.

[22] F. T. L. Muniz, M. A. R. Miranda, C. M. dos Santos, and J. M. Sasaki. "The Scherrer equation and the dynamical theory of X-ray diffraction.". *Acta Crystallogr*, **72**:385–90, 2016. DOI: https://doi.org/10.1107/S205327331600365X.

[23] A. Hassanien, A. A. Akl, and A. Sáaedi. "Synthesis, crystallography, microstructure, crystal defects, and morphology of Bix Zn1-xO nanoparticles prepared by sol-gel technique.". *Cryst. Eng. Comm.*, **20**:1716–1730, 2018. DOI: https://doi.org/10.1039/c7ce02173a.

[24] F. A. Akgul, G. Akgul, N. Yildirim, H. E. Unalan, and R. Turan. "Influence of thermal annealing on microstructural, morphological, optical properties and surface electronic structure of copper oxide thin films. ". *Mat. Chem. Phys.*, **147**:987–995, 2014. DOI: https://doi.org/10.1016/j.matchemphys.2014.06.047.

[25] M. Shaban, M. Zayed, and H. Hamdy. "Nanostructured ZnO thin films for self-cleaning applications.". *RSC Adv*, **7**:617–631, 2017. DOI: https://doi.org/10.1039/C6RA24788A.

[26] K. Ravichandran, P. V. Rajkumar, B. Sakthivel, K. Swaminathan, and L. Chinnappa. "Role of precursor material and annealing ambience on the physical properties of SILAR deposited ZnO films. ". *Ceramics International*, **40**:12375–12382, 2014. DOI: https://doi.org/10.1016/j.ceramint.2014.04.086.

[27] S. C. Sami and H. M. Tahseen. "The effect of Ti on physical properties of Fe_2O_3 thin films for gas sensor applications. ". *International Journal of Nano electronics and Materials*, **13**:221–232, 2020.

[28] S. AL-Dahaan, A. Al-khayatt, and M. Salman. "The optical properties of Fe_2O_3 thin film prepared by chemical spray pyrolysis deposition (CSP).". *Journal of Kufa–Physics*, **6**, 2014.

[29] H. K. Essa, A. A. Khadayeir, H. T. Salloom, N. F. Habubi, and S. S. Chiad. "Physical Properties of Nanostructured Fe_2O_3 Thin films Effect of Cobalt Doping Depositedby CSP. ". *Journal of Physics: Conference Series, IOP Science*, **199**, 2021. DOI: https://doi.org/10.1088/1742-6596/1999/1/012062.

[30] J. M. Rzaij and N. F. Habubi. "Enhancing the CO_2 sensor response of nickel oxide-doped tin dioxide thin films synthesized by SILAR method. ". *Journal of Materials Science: Materials in Electronics*, **33**:11851–11863, 2022. DOI: https://doi.org/10.1007/s10854-022-08148-2.

[31] H. Mansour, H. Letifi, R. Bargougui, S. De Almeida-Didry, B. Negulescu, C. Autret-Lambert, and S. Ammar. "Structural, optical, magnetic and electrical properties of hematite (α-Fe_2O_3) nanoparticles synthesized by two methods: polyol and precipitation.". *Applied Physics A*, **123**:787, 2017. DOI: https://doi.org/10.1007/s00339-017-1408-1.

[32] E. S. Hassan, T. H. Mubarak, S. S. Chiad, N. F. Habubi, A. A. Khadayeir, M. O. Dawood, and I. A. Al-Baidhany. "Physical Properties of indium doped Cadmium sulfide thin films prepared by (SPT).". *Journal of Physics: Conference Series*, **1294** , 2019. DOI: https://doi.org/10.1088/1742-6596/1294/2/022008.

[33] N. Y. Ahmed, B. A. Bader, M. Y. Slewa, N. F. Habubi, and S. S. Chiad. "Effect of boron on structural, optical characterization of nanostructured Fe_2O_3 thin films.". *Neuro Quantology*, **18**:55, 2020. DOI: https://doi.org/10.14704/nq.2020.18.6.NQ20183.

[34] J. Klein, L. Kampermann, B. Mockenhaupt, M. Behrens, J. Strunk, and G. Bacher. "Limitations of the Tauc plot method.". *Adv. Funct. Mater.*, **33** :2304523, 2023. DOI: https://doi.org/10.1002/adfm.202304523.

[35] S. G. Ruvalcaba-Manzo, S. J. Castillo, M. Flores-Acosta, R. Ochoa-Landín, and R. Ramírez-Bon. "Study of optical, morphological, structural, and chemical properties of CdO thin films synthesized by thermal annealing transformation of $CdCO_3$ thin films. ". *Optical Materials*, **132**:112742, 2022. DOI: https://doi.org/10.1016/j.optmat.2022.112742.

[36] S. J. Ikhmayies and R. N. Ahmad-Bitar. "A study of the optical bandgap energy and Urbach tail of spray-deposited CdS:In thin films. ". *Journal of Materials Research and Technology*, **2**:221–227, 2013. DOI: https://doi.org/10.1016/j.jmrt.2013.02.012.